Submitted to *Science Bulletin*

Supplementary Information

Complete three-dimensional coseismic displacements related to the 2021 Maduo earthquake in Qinghai province, China from Sentinel-1 and ALOS-2 SAR images

Jihong Liu[1], Jun Hu[1,*], Zhiwei Li[1], Zhangfeng Ma[2], Lixin Wu[1], Weiping Jiang[3], Guangcai Feng[1], Jianjun Zhu[1]

[1] *School of Geosciences and Info-Physics, Central South University, Changsha 410083, Hunan, China*

[2] *School of Earth Sciences and Engineering, Hohai University, Nanjing 211100, Jiangsu, China*

[3] *GNSS Research Center, Wuhan University, Wuhan 430079, China*

Text

Text S1. SAR data processing

For a pair of SAR images, the DInSAR method is usually the first choice for measuring the ground surface displacement, which is the projection of real 3-D displacements along the LOS direction. Currently, since most of SAR data are acquired by the near-polar orbit satellites in the right-looking imaging mode, the DInSAR-derived displacements are only available in two distinct geometries (i.e., ascending and descending LOS directions), and cannot well constrain the real 3-D displacements, especially for the north-south displacement component. The MAI, POT, and BOI methods can all derive the displacement observation along the satellite AZI direction. Since the AZI direction is almost parallel to the N-S direction, the AZI displacement observations derived by these three methods can well make up for the missing N-S displacement information in the LOS displacement observations. Although the BOI-obtained AZI observations are only available in the burst overlaps of Sentinel-1 SAR data, when other AZI observations are not available, they would provide the very important information for constraining the real 3-D displacements [1].

In general, compared to the MAI, POT, and BOI methods, the DInSAR method has the highest displacement observation accuracy, ranging from centimeters to millimeters [2]. Since MAI and BOI methods rely on the phase information of SAR data, their displacement observation accuracy is usually believed to be higher than the accuracy of amplitude-based POT displacement observations [1, 3]. Although the basic principle of the BOI and MAI methods are very similar, the BOI method is usually considered to be more accurate than the MAI method since the squint angle differences of the SAR data used in BOI method is generally larger than those in MAI method [1]. It should be noted that the accuracy of POT method is highly dependent on the pixel resolution [4]. If the pixel resolution of SAR data is very high (e.g., TerraSAR-X/TanDEM-X), it is possible that the POT accuracy is comparable with or even higher than the MAI/BOI methods.

Besides, since the DInSAR, MAI, and BOI methods rely on the phase information, they are susceptible to the decorrelation noise. For the monitoring of coseismic displacement, these phase-based methods are often unable to obtain effective observations in the fault rupture region. However, due to the employment of SAR amplitude information, the POT method is generally capable of deriving the complete displacement field even in the fault rupture region, providing valuable data for constraining the fault slip model and interpretating the behavior of near-surface fault movement.

Since the Sentinel-1 data has a limited azimuth spatial resolution and doppler bandwidth, the MAI method is not

employed to process the Sentinel-1 SAR data. The BOI processing is only applicable to the TOPS-mode Sentinel-1 SAR data. In addition to the SAR data, the shuttle radar topographic mission (SRTM) 1-arc- second (~30 m spacing) digital elevation model (DEM) is used here to remove the topographic contributions and assist in the co-registration process. The Sentinel-1, ascending strip-map-mode ALOS-2, and descending ScanSAR-mode ALOS-2 SAR images were multi-looked by 8×30, 8×20, and 5×32 (range×azimuth), respectively, which resulted in a final resolution of approximately 100 m × 100 m for all displacement observations. For the sake of simplicity, the combination of several abbreviations linked by underlines is used to represent the corresponding SAR displacement observation. For example, ALOS2_AS_DInSAR represents the DInSAR observation of ascending (AS) ALOS-2 data, S1_DES_POT_AZI represents the POT observation of Descending (DES) Sentine1-1 (S1) data along the AZI direction, and S1_DInSAR represents the DInSAR observations of S1 data from both ascending and descending orbits.

S1.1. DInSAR processing

After the co-registration process and the generation of differential interferogram, an improved Goldstein filter [5] is used to minimize the decorrelation noise. Before unwrapping the filtered interferograms by the minimum cost flow method [6], an unwrapping mask file is generated with the coherence value smaller than 0.8, and some isolated pixels are manually masked to avoid possible unwrapping errors. For the S1 interferograms, since the interferometric phase is continuous across the interferogram and the shorter wavelength of SAR data is less affected by the ionospheric delay [7], it is easy to realize the phase unwrapping and obtain a reliable displacement field (Fig. S1(a) and Fig. S1(e)). However, for the ascending ALOS-2 interferogram, since the displacement field is divided into two parts by the fault (Fig. S1(i)) and the original interferogram contains obvious ionospheric signals, it is impossible to obtain reliable deformation results directly. Fortunately, the coverage of this interferogram is relatively small, making it possible to fit and remove the ionospheric signals by polynomials. Therefore, to obtain a reliable DInSAR displacement field, the ionospheric signal-corrected ALOS2_AS_POT_LOS observation is employed to assist the phase unwrapping and the ionospheric signal correction of the isolated two parts in the ascending ALOS-2 DInSAR interferogram. For the descending ALOS-2 interferogram, which consists of five separate beams, the coverage is larger than one standard Sentinel-1 image, so it is difficult to remove the present ionospheric phase by polynomial fitting. Here, each beam is separately processed based on the standard DInSAR workflow, then mosaiced together in the geographical coordinate system. To correct the ionospheric delay, a range split-spectrum (RSS) method [8, 9] is employed for each beam. However, since the RSS method is very sensitive to the coherence, the RSS-derived ionospheric phases show strong fluctuations in the low-coherence near-fault region (e.g., Fig. 3(b)), which can seriously degrade the accuracy of the displacement observations. In this paper, we propose a polynomial fitting (PolyFit) method to mitigate these strong ionospheric fluctuations (see the main text). Fig. S2 shows the ALOS2_DES_DInSAR observation before and after the ionospheric delay correction based on the PolyFit method, where the ionospheric phases have been significantly mitigated.

S1.2. POT processing

The POT method maps the ground displacements along both the AZI and LOS directions based on a subpixel correlation technique to the SAR amplitude images [4]. Prior to the standard POT workflow, the Sentinel-1 single look complex (SLC) images should be deramped [10]. The matching window sizes of 128×128 pixels with the oversampling factor of two is employed for all the SAR data. Each beam of descending ALOS-2 data is separately processed and then mosaicked based on the displacements in the beam overlap area. A second-order polynomial is employed to fit the possible orbit ramp based on signals in the far-field regions. As shown in Fig. S1, the S1_POT observations can substantially reveal the coseismic displacements. In particular, the S1_POT_LOS observations

(Fig. S1(b) and Fig. S1(f)) can clearly reveal the fault traces. As shown in Fig. S1(b) and Fig. S1(f), around the east of the main fault, there is another one small fault that obviously ruptured the surface. These fault traces can only be clearly observed in the POT observations compared to the DInSAR/MAI/BOI observations, illuminating that the POT method is significant for studying the earthquake displacements. Since the POT accuracy is highly dependent on the pixel spatial resolution, the S1_POT_LOS observations (Fig. S1(b) and Fig. S1((f)) are more reliable than the S1_POT_AZI observations (Fig. S1(c) and Fig. S1(g)). Besides, the S1_DES_POT_AZI (Fig. S1(g)) is much noisier than the S1_AS_POT_AZI (Fig. S1(c)), which could be attributed to the longer spatial perpendicular baseline (see Table 1) for the descending SAR images pair. While for the ALOS-2 data, significant ionospheric signals exist in the ALOS2_POT_AZI observations (Fig. S1(k) and Fig. S1(o)), which basically mask the displacement signals. In addition, due to the reduced range pixel resolution of ALOS-2 ScanSAR data compared to the ALOS-2 strip-map data, the ALOS2_DES_POT_LOS (Fig. S1(n)) is much noisier than the ALOS2_AS_POT_LOS (Fig. S1(j)).

S1.3. MAI processing

The MAI method [3] applies the split-beam InSAR processing to extract the AZI displacements, in which the full-aperture SLC images are separated into two sub-apertures, i.e., the forward and backward apertures . Based on four sub-aperture SLCs, backward-looking and forward-looking interferograms can be generated using the standard DInSAR method. The azimuth displacement is then obtained by differencing these two sub-aperture interferograms. Given that the ALOS-2 SAR data used in this paper suffers serious ionospheric delays that have a greater effect on the AZI observations, the ALOS2_MAI observations (Fig. S1(l) and Fig. S1(p)), similar to the ALOS2_POT_AZI observations (Fig. S1(k) and Fig. S1(o)), are contaminated by the undesirable strip-shape ionospheric phases.

S1.4. BOI processing

Taking the advantages of the large squint angle diversity for Sentinel-1 two adjacent bursts in the burst overlap region, it is feasible to derive the AZI displacements in the overlap regions [1]. The overlap region is about 8.6 km×1.5 km and accounts for about 7.5% of a burst along the AZI direction. The basic principles of the BOI and MAI methods are very similar. In the overlap region, the SAR data acquired by the two adjacent bursts can be considered as the backward-looking and forward-looking SLC images. To obtain the AZI displacements, the main steps of the BOI method include the generation of backward-looking and forward-looking interferograms and the differential processing between these two interferograms. After the precise co-registration of a pair of Sentinel-1 data, four SLC images in a target burst overlap region can be obtained based on the azimuth line time. The backward and forward interferograms can be generated by simply conjugate multiplication for the two backward SLCs and the two forward SLCs, respectively. Subsequently, the AZI displacement phase can be derived by the conjugate multiplication between these two interferograms[1]. Here, the improved Goldstein filter [5] is employed to mitigate the decorrelation noise. With respect to the geographical coordinate of these BOI observations, it is not recommended to conduct the geocoding process separately for each burst overlap region since it is hardly to realize the precise co-registration between the external DEM data and such a limited range of SAR data. Alternatively, the geocoding process can be precisely realized for the whole region of SAR data, therefore the geographical coordinate for the whole SAR images can be accurately determined. In this case, the geographical coordinate of these overlap regions can be extract from the geographical coordinate of the whole SAR images.

As shown in Fig. S1, the BOI observations can clearly reveal the coseismic displacements across the faults. Since the AZI direction of the ascending Sentinel-1 data is closer to the direction of the coseismic horizontal displacements, the S1_AS_BOI displacements (Fig. S1(d)) are more obvious than the S1_DES_BOI displacements (Fig. S1(h)). Besides, the spatial pattern and the displacement magnitude between the S1_BOI and the

S1_POT_AZI observations are very similar, demonstrating the validation of these observations.

Text S2. The SM-VCE method

Sixteen displacement observations are derived based on the Sentinel-1/ALOS-2 SAR data and the DInSAR/POT/MAI/BOI methods. However, due to the contamination of severe ionosphere disturbances and the decorrelation noise, the S1_DES_POT_AZI (Fig. S1(g)), ALOS2_AS_POT_AZI (Fig. S1(k)), ALOS2_AS_MAI (Fig. S1(l)), ALOS2_DES_POT_AZI (Fig. S1(o)), and ALOS2_DES_MAI (Fig. S1(p)) observations are excluded and only the rest eleven displacement observations are used in the following 3-D displacement estimation process.

There is no doubt that such a wealth of observations helps in geophysical analysis of the earthquake, but accompanying difficulties cannot be overlooked. For example, in the quantitative model inversion process, there must be a trade-off between model accuracy and inverting efficiency. If all available displacement observations are used, the inverting computational burden would be very high. One possible solution that can significantly decrease the computational burden without much compromise of accuracy is to only reserve one observation among those with similar geometry. For example, since the geometry of ascending DInSAR observations and ascending POT LOS observations for Sentinel-1 and ALOS-2 is very similar, we can select one of these observations for the model inversion and discard the rest. However, this solution is susceptible to missing some valuable information. If the DInSAR observations are select, the near-fault POT displacement observations are missing; if the POT observations are selected, the higher accuracy of far-field DInSAR observations are useless.

Besides, these displacement observations in Fig. S1 are only 1-D displacement projections of the real 3-D displacements along a particular direction (e.g., LOS and AZI) and can't be directly used to interpret the real fault movements. Three-dimensional displacements (i.e., east-west, north-south, and vertical) represents a combination of minimum number of displacement components that can vividly describe the real surface movements. Therefore, if a reliable 3-D displacements field can be obtained by combining the multiple available SAR displacement observations, the above problems (e.g., the trade-off between accuracy and efficiency in the model inversion process, and the poor interpretability of SAR displacement observations) can be avoided.

Here, the recently proposed SM-VCE method is employed to estimate the 3-D displacements of the 2021 Maduo earthquake. For completeness, this section introduces the basic principles of the SM-VCE method.

Based on the SM, a portion of Earth's surface, deformed by a geodynamic process (e.g., earthquake), can be regarded as a homogeneous strain field [11-13]. We suppose that a target point P^0, with 3-D position components $\boldsymbol{x}^0 = [x_e^0 \quad x_n^0 \quad x_v^0]^T$ and 3-D displacement components $\boldsymbol{d}^0 = [d_e^0 \quad d_n^0 \quad d_v^0]^T$, is surrounded by K points $P^k (k = 1, 2 \dots K)$ in a window, whose 3-D position and displacement components are $\boldsymbol{x}^k = [x_e^k \quad x_n^k \quad x_v^k]^T$ and $\boldsymbol{d}^k = [d_e^k \quad d_n^k \quad d_v^k]^T$, respectively. Superscripts e, n, v denote east-west, north-south and vertical components, respectively.

Assuming $\Delta^k = \boldsymbol{x}^k - \boldsymbol{x}^0 = [\Delta x_e^k \quad \Delta x_n^k \quad \Delta x_v^k]^T$ denotes the coordinate-increment vector from the point P^0 to the point P^k, the relationship between $\boldsymbol{d}^k$ and $\boldsymbol{d}^0$ can be represented as

$$\boldsymbol{d}^k = \boldsymbol{H} \cdot \Delta^k + \boldsymbol{d}^0 \tag{S1}$$

where $\boldsymbol{H} = \boldsymbol{S} + \boldsymbol{R}$ is the displacement gradient matrix, and $\boldsymbol{S}$ and $\boldsymbol{R}$, the symmetric and antisymmetric parts, can be respectively written as [11]

$$\boldsymbol{S} = \begin{bmatrix} \xi_{ee} & \xi_{en} & \xi_{ev} \\ \xi_{en} & \xi_{nn} & \xi_{nv} \\ \xi_{ev} & \xi_{nv} & \xi_{vv} \end{bmatrix} \tag{S2}$$

$$\boldsymbol{R}=\begin{bmatrix}0 & -\omega_{en} & \omega_{ev}\\ \omega_{en} & 0 & -\omega_{nv}\\ -\omega_{ev} & \omega_{nv} & 0\end{bmatrix} \tag{S3}$$

According to Eq. (S1), the observation function between unknown vector $\boldsymbol{l}$ and $\boldsymbol{d}^k$ can thus be modeled as

$$\boldsymbol{d}^k=\boldsymbol{B}_{\mathrm{sm}}^k\cdot\boldsymbol{l} \tag{S4}$$

where $\boldsymbol{l}=[d_e^0 \quad d_n^0 \quad d_v^0 \quad \xi_{ee} \quad \xi_{en} \quad \xi_{ev} \quad \xi_{nn} \quad \xi_{nv} \quad \xi_{vv} \quad \omega_{en} \quad \omega_{ev} \quad \omega_{nv}]^T$, ξ and ω represent the parameters of strain tensor and rigid body rotation tensor, respectively. The design matrix $\boldsymbol{B}_{\mathrm{sm}}^k$ can be expressed as

$$\boldsymbol{B}_{\mathrm{sm}}^k=\begin{bmatrix}1 & 0 & 0 & \Delta x_e^k & \Delta x_n^k & \Delta x_v^k & 0 & 0 & 0 & -\Delta x_n^k & \Delta x_v^k & 0\\ 0 & 1 & 0 & 0 & \Delta x_e^k & 0 & \Delta x_n^k & \Delta x_v^k & 0 & \Delta x_e^k & 0 & -\Delta x_v^k\\ 0 & 0 & 1 & 0 & 0 & \Delta x_e^k & 0 & \Delta x_n^k & \Delta x_v^k & 0 & -\Delta x_e^k & \Delta x_n^k\end{bmatrix} \tag{S5}$$

Assuming that there is an observation vector $\boldsymbol{L}^k=\left[L_1^k,L_2^k,\dots,L_j^k,\dots,L_J^k\right]^T$ that is consist with the InSAR observations at point P^k, and the subscripts $1,2,\dots,j,\dots,J$ represent the indexes of J types of available observations (e.g., ascending/descending displacement observations along the LOS and AZI directions). The relationship between the 3-D deformation components d^k and the observation vector L^k can be represented by

$$\boldsymbol{L}^k=\boldsymbol{B}_{\mathrm{geo}}^k\cdot\boldsymbol{d}^k \tag{S6}$$

where $\boldsymbol{B}_{\mathrm{geo}}^k$ is the transform matrix which can be expressed as

$$\boldsymbol{B}_{\mathrm{geo}}^k=\left[\left(\boldsymbol{B}_{\mathrm{geo},1}^k\right)^T,\left(\boldsymbol{B}_{\mathrm{geo},2}^k\right)^T,\dots,\left(\boldsymbol{B}_{\mathrm{geo},j}^k\right)^T,\dots,\left(\boldsymbol{B}_{\mathrm{geo},J}^k\right)^T\right]^T \tag{S7}$$

and $\boldsymbol{B}_{\mathrm{geo},j}^k=\left[a_j^k \quad b_j^k \quad c_j^k\right],(j=1,2,\dots,J)$ is a unit vector that projects the 3-D displacements at point P^k to the corresponding direction of the *j*th observations (e.g., LOS and AZI directions), where

$$\begin{cases} a_j^k=-\mathrm{flag}\cdot sin\left(\theta_j^k\right)\cdot cos\left(\alpha_j^k\right)\\ b_j^k=\mathrm{flag}\cdot sin\left(\theta_j^k\right)\cdot sin\left(\alpha_j^k\right)\\ c_j^k=cos\left(\theta_j^k\right)\\ \mathrm{flag}=\begin{cases}-1, & \mathrm{left-looking\ mode}\\ 1, & \mathrm{right-looking\ mode}\end{cases}\end{cases} \quad \text{or} \quad \begin{cases}a_j^k=sin\left(\alpha_j^k\right)\\ b_j^k=\cos\left(\alpha_j^k\right)\\ c_j^k=0\end{cases} \tag{S8}$$

when the L_j^k represents the displacement observation along the LOS or AZI direction. α_j^k and θ_j^k are the satellite heading angle (clockwise from the north) and the radar incidence angle of the point P^k, respectively.

By combining Eqs. (S4) and (S6), the relationship between the unknown vector $\boldsymbol{l}$ and the InSAR observations $\boldsymbol{L}^k$ can be formed as

$$\boldsymbol{L}^k=\boldsymbol{B}^k\cdot\boldsymbol{l} \tag{S9}$$

where $\boldsymbol{B}^k=\boldsymbol{B}_{\mathrm{geo}}^k\cdot\boldsymbol{B}_{\mathrm{sm}}^k$

$$=\begin{bmatrix}a_1^k & b_1^k & c_1^k & a_1^k\Delta x_e^k & a_1^k\Delta x_n^k+b_1^k\Delta x_e^k & a_1^k\Delta x_v^k+c_1^k\Delta x_e^k & b_1^k\Delta x_n^k & b_1^k\Delta x_v^k+c_1^k\Delta x_n^k & c_1^k\Delta x_v^k & -a_1^k\Delta x_n^k+b_1^k\Delta x_e^k & a_1^k\Delta x_v\\ a_2^k & b_2^k & c_2^k & a_2^k\Delta x_e^k & a_2^k\Delta x_n^k+b_2^k\Delta x_e^k & a_2^k\Delta x_v^k+c_2^k\Delta x_e^k & b_2^k\Delta x_n^k & b_2^k\Delta x_v^k+c_2^k\Delta x_n^k & c_2^k\Delta x_v^k & -a_2^k\Delta x_n^k+b_2^k\Delta x_e^k & a_2^k\Delta x_v\\ & & & & & & \vdots & & & & \\ a_J^k & b_J^k & c_J^k & a_J^k\Delta x_e^k & a_J^k\Delta x_n^k+b_J^k\Delta x_e^k & a_J^k\Delta x_v^k+c_J^k\Delta x_e^k & b_J^k\Delta x_n^k & b_J^k\Delta x_v^k+c_J^k\Delta x_n^k & c_J^k\Delta x_v^k & -a_J^k\Delta x_n^k+b_J^k\Delta x_e^k & a_J^k\Delta x_v\end{bmatrix}$$

For K_j surrounding points of P^0 for the *j*th type of observation, the overall observation system can be constructed based on Eq. (S9)

$$\boldsymbol{L}=\boldsymbol{B}\cdot\boldsymbol{l} \tag{S10}$$

where the observation vector $\boldsymbol{L}$ with size of $\sum_1^J K_j\times 1$ and the coefficient matrix $\boldsymbol{B}$ with size of $\sum_1^J K_j\times 12$

can be respectively represented by

$$\boldsymbol{L} = \left[(\boldsymbol{L}_1)^T, (\boldsymbol{L}_2)^T \dots (\boldsymbol{L}_J)^T\right]^T \tag{S11}$$

$$\boldsymbol{B} = \left[(\boldsymbol{B}_1)^T, (\boldsymbol{B}_2)^T \dots (\boldsymbol{B}_J)^T\right]^T \tag{S12}$$

After the establishment of the observation system (Eq. (S10)), the VCE algorithm can be employed to determine the weight of each displacement observations. Like Eq. (S6), the observation system (Eq. (S10)) can be divided into J groups. For the sake of simplicity, we assume that the initial weight matrix of each group of observations $\boldsymbol{W}_j$ are equal to unit matrix with size of $K_j \times K_j$. $\boldsymbol{L}_j$ and $\boldsymbol{B}_j$ $(j = 1, 2, \dots, J)$ correspond to the observation and design matrix of the jth group, which can be extracted from $\boldsymbol{L}$ and $\boldsymbol{B}$ (i.e., Eqs. (S11) and (S12)), respectively. Assuming that $\boldsymbol{N}_j = \boldsymbol{B}_j^T \boldsymbol{W}_j \boldsymbol{B}_j, \boldsymbol{U}_j = \boldsymbol{B}_j^T \boldsymbol{W}_j \boldsymbol{L}_j$, and $\boldsymbol{N} = \sum_{j=1}^{J} \boldsymbol{N}_j, \boldsymbol{U} = \sum_{j=1}^{J} \boldsymbol{U}_j$, the WLS solution of the unknown vector $\boldsymbol{l}$ is

$$\boldsymbol{l} = \boldsymbol{N}^{-1}\boldsymbol{U} \tag{S13}$$

Subsequently, the relationship between the observation residuals $\boldsymbol{\delta}$ and the variance components $\hat{\boldsymbol{\sigma}}^2$ can be constructed as [14]

$$\hat{\boldsymbol{\sigma}}^2 = \boldsymbol{\Gamma}^{-1}\boldsymbol{\delta} \tag{S14}$$

where

$$\hat{\boldsymbol{\sigma}}^2 = \left[\hat{\sigma}_1^2, \hat{\sigma}_2^2, \dots, \hat{\sigma}_j^2, \dots, \hat{\sigma}_J^2\right]^T$$

$$\boldsymbol{\Gamma} = \begin{bmatrix} K_1 - 2tr(\boldsymbol{N}^{-1}\boldsymbol{N}_1) + tr(\boldsymbol{N}^{-1}\boldsymbol{N}_1)^2 & tr(\boldsymbol{N}^{-1}\boldsymbol{N}_1\boldsymbol{N}^{-1}\boldsymbol{N}_2) & \cdots & tr(\boldsymbol{N}^{-1}\boldsymbol{N}_1\boldsymbol{N}^{-1}\boldsymbol{N}_J) \\ tr(\boldsymbol{N}^{-1}\boldsymbol{N}_2\boldsymbol{N}^{-1}\boldsymbol{N}_1) & K_2 - 2tr(\boldsymbol{N}^{-1}\boldsymbol{N}_2) + tr(\boldsymbol{N}^{-1}\boldsymbol{N}_2)^2 & \cdots & tr(\boldsymbol{N}^{-1}\boldsymbol{N}_2\boldsymbol{N}^{-1}\boldsymbol{N}_J) \\ \vdots & \vdots & \ddots & \vdots \\ tr(\boldsymbol{N}^{-1}\boldsymbol{N}_J\boldsymbol{N}^{-1}\boldsymbol{N}_1) & tr(\boldsymbol{N}^{-1}\boldsymbol{N}_J\boldsymbol{N}^{-1}\boldsymbol{N}_2) & \cdots & K_J - 2tr\left(\boldsymbol{N}^{-1}\boldsymbol{N}_J\right) + tr\left(\boldsymbol{N}^{-1}\boldsymbol{N}_J\right)^2 \end{bmatrix}$$

$$\boldsymbol{\delta} = \left[\boldsymbol{r}_1^T\boldsymbol{W}_1\boldsymbol{r}_1, \boldsymbol{r}_2^T\boldsymbol{W}_2\boldsymbol{r}_2, \dots, \boldsymbol{r}_j^T\boldsymbol{W}_j\boldsymbol{r}_j, \dots, \boldsymbol{r}_J^T\boldsymbol{W}_J\boldsymbol{r}_J\right]^T$$

$$\boldsymbol{r}_j = \boldsymbol{B}_j \cdot \boldsymbol{l} - \boldsymbol{L}_j$$

The variance components $\hat{\boldsymbol{\sigma}}^2$ are also exploited to update the weight matrixes of the J groups of InSAR observations

$$\widehat{\boldsymbol{W}}_j = \frac{\hat{\sigma}_1^2}{\hat{\sigma}_j^2 \boldsymbol{W}_j^{-1}} \tag{S15}$$

The updated weight matrixes $\widehat{\boldsymbol{W}}_j$ in Eq. (S13) are then used in Eqs. (S13)-(S15) to iteratively update the weights until the following formula is satisfied

$$\hat{\sigma}_{max}^2 - \hat{\sigma}_{min}^2 \le \tau^2 \tag{S16}$$

where $\hat{\sigma}_{max}^2$ and $\hat{\sigma}_{min}^2$ are the maximum and minimum of the variance components $\hat{\boldsymbol{\sigma}}^2 = \left[\hat{\sigma}_1^2, \hat{\sigma}_2^2, \dots, \hat{\sigma}_j^2, \dots, \hat{\sigma}_J^2\right]^T$, respectively. τ^2 is the convergence criteria, which can be determined based on the general accuracies of observations. In this study, $\tau^2 = 1.0 \times 10^{-4}$ since the accuracy of POT-derived displacement observation is generally at the level of centimeter [15]. Finally, the 3-D displacement components are determined from Eq. (S13) with the weight matrices from the final iteration.

Text S3. The calculation of three strain invariants

The dilatation ε_1, the differential rotation ε_2, and the maximum shear ε_3 can be determined based on the parameters in the strain model (i.e., ξ and ω in Eqs. S2 and S3) by the following equations [30]

$$\varepsilon_1 = \xi_{ee} + \xi_{nn} \tag{S17}$$

$$\varepsilon_2 = \omega_{en} \tag{S18}$$

$$\varepsilon_3 = \sqrt{\frac{1}{4}(\xi_{ee} - \xi_{nn})^2 + \xi_{en}} \tag{S19}$$

Besides, the maximum and minimum normal strains $\lambda_{\max}$, $\lambda_{\min}$ and the direction $\theta_{\lambda_{\max}}$ (clockwise from the north) of the $\lambda_{\max}$ can be obtained as follows [30]

$$\lambda_{\max} = \frac{1}{2}(\xi_{ee} + \xi_{nn}) + \varepsilon_3 \tag{S20}$$

$$\lambda_{\min} = \frac{1}{2}(\xi_{ee} + \xi_{nn}) - \varepsilon_3 \tag{S21}$$

$$\theta_{\lambda_{\max}} = \frac{1}{2} arctan\left(\frac{\xi_{nn} - \xi_{ee}}{2\xi_{en}}\right) \tag{S22}$$

The angle that the maximum shear direction makes with the maximum normal strain axis can be determined by [23]

$$\theta_{\varepsilon_3,\lambda_{\max}} = arctan\left(sign(\frac{\lambda_{\min}}{\lambda_{\max}}) \cdot \sqrt{\left|\frac{\lambda_{\min}}{\lambda_{\max}}\right|}\right) \tag{S23}$$

where $sign$ is the signum function. Therefore, the direction θ_{ε_3} (clockwise from the north) of the maximum shear ε_3 can be obtained by [23]

$$\theta_{\varepsilon_3} = \theta_{\lambda_{\max}} + \theta_{\varepsilon_3,\lambda_{\max}} \tag{S24}$$

Since the strain model parameters and 3-D displacements can be simultaneously calculated by the SM-VCE method, the above variables in Eqs. (S17)-(S24) can be directly calculated after the SM-VCE method.

Text S4. The Detailed Geodetic Inversion Process

In this text section, we aimed to give a detailed description on our geodetic inversion constrained by 3-D displacements. The inversion process can be divided into three steps.

The first step is to determine the fault geometry. According to our derived 3-D displacement map. Based on visual inspection of the interferograms, the interferometric coherence maps, and the deformation map calculated by offset-tracking, we infer that there are two potential faults and we extracted the fault trace from these maps. Therefore, the strike direction can be determined. Before determining dipping angles, we assume that these two faults have their own different dipping angles. We first discretized the long fault into irregular rectangle using a geometric progression method [16] and we mesh these rectangles into triangle dislocations using mesh2d software (https://www.mathworks.com/matlabcentral/fileexchange/25555-mesh2d-delaunay-based-unstructured-mesh-generation). We calculated the optimal dipping angle using the trade-off curve method (Fig. S7). Then we discretized the short fault and calculated the optimal dipping angle (Fig. S7(b)).

In the second step, we use an adaptive downsampling method to resample our derived 3D deformation into several

triangles (Fig. S8) [17, 18].

In the third step, we generate the green function based on the our inferred fault geometry [19]. A recursive constrained linear least squares method is used to approach the final slip distribution. In inversion, we perform a second order Laplacian operator to constrain the model smoothness. Moreover, we automatically select the optimal model smooth factor (Fig. S11) through searching for the position of maximum curvature in L-curve [20], which represents a trade-off between the slip smoothness and realistic of slip.

Text S5. The Bootstrapping Test for Deriving Slip Model Uncertainty

To explore the uncertainty of the inversion results due to possible random errors in our derived slip distribution, we implemented a bootstrapping test method [21]. Through this method, we repeated the geodetic inversion process 100 times, in each iteration adding a white noise with zero mean and 5 cm standard deviation to our derived 3-D displacements in each repetition. We calculated the standard deviation of 100 times results and treated it as the model uncertainty (Fig. S10).

Figures

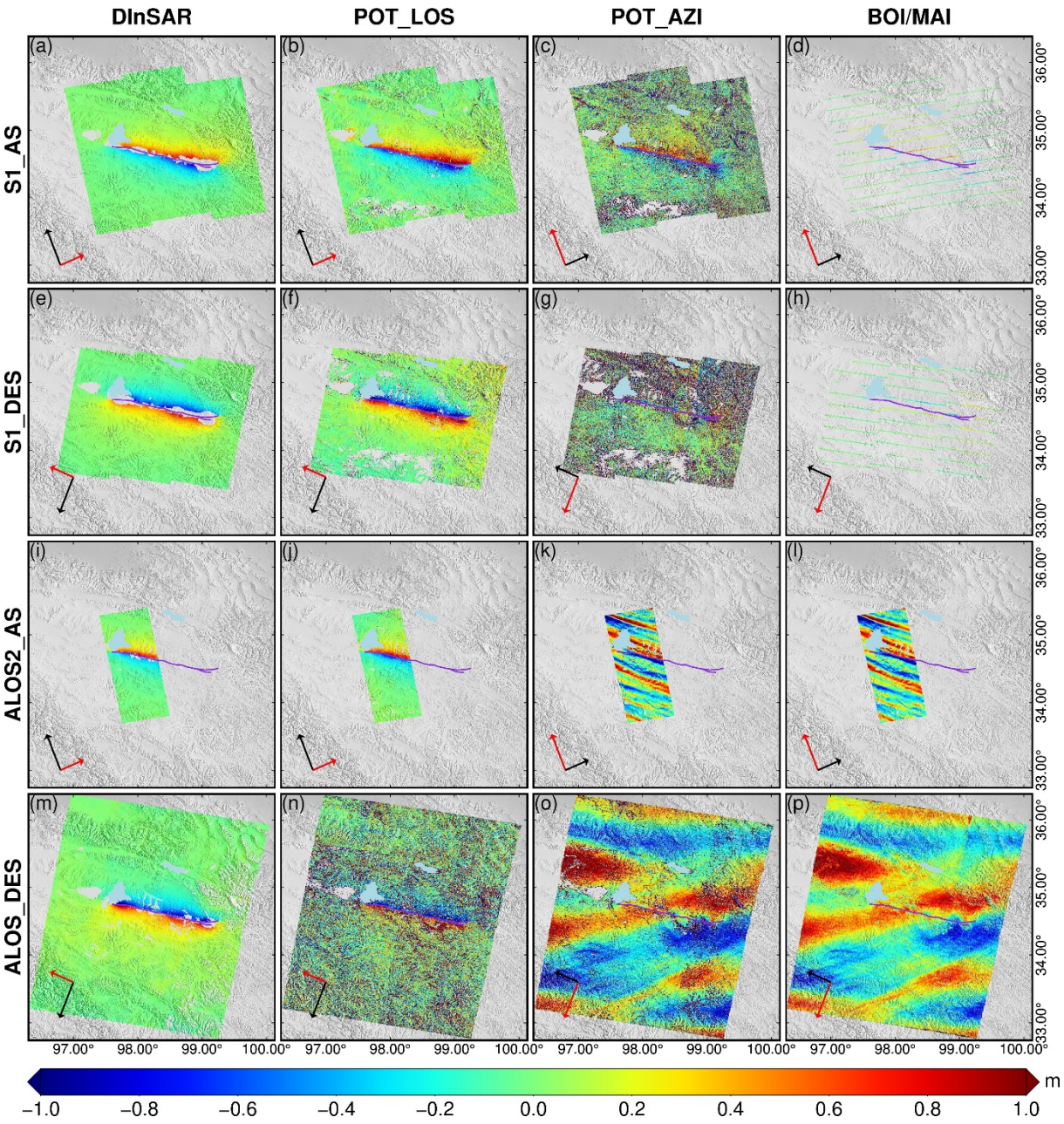

Fig. S1. Displacement observations over the whole SAR images along the LOS and AZI directions from ascending/descending, S1/ALOS-2 SAR data based on the DInSAR, POT, MAI and BOI methods. Longer and shorter arrows represent the AZI and LOS directions, respectively, and the red arrow corresponds to the observing direction of each observation. The purple lines show the location of ruptured fault traces. The enlarged view of the displacements near the fault can be found in the main text.

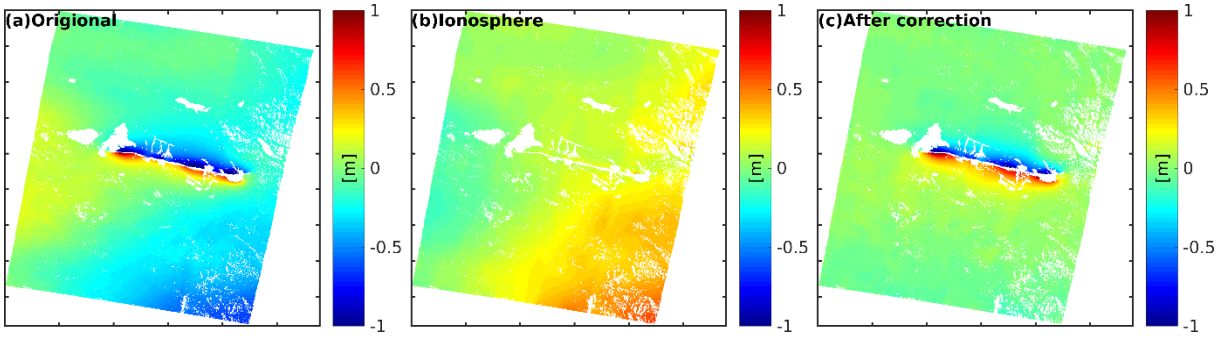

Fig. S2. (a) The original unwrapped descending ALOS-2 DInSAR observation. (b) The ionospheric delay optimized by the proposed filtering and interpolating strategy based on the result of the range spectrum split method. (c) (a)-(b). As can be seen, the ionospheric delay can be largely mitigated based on the proposed method.

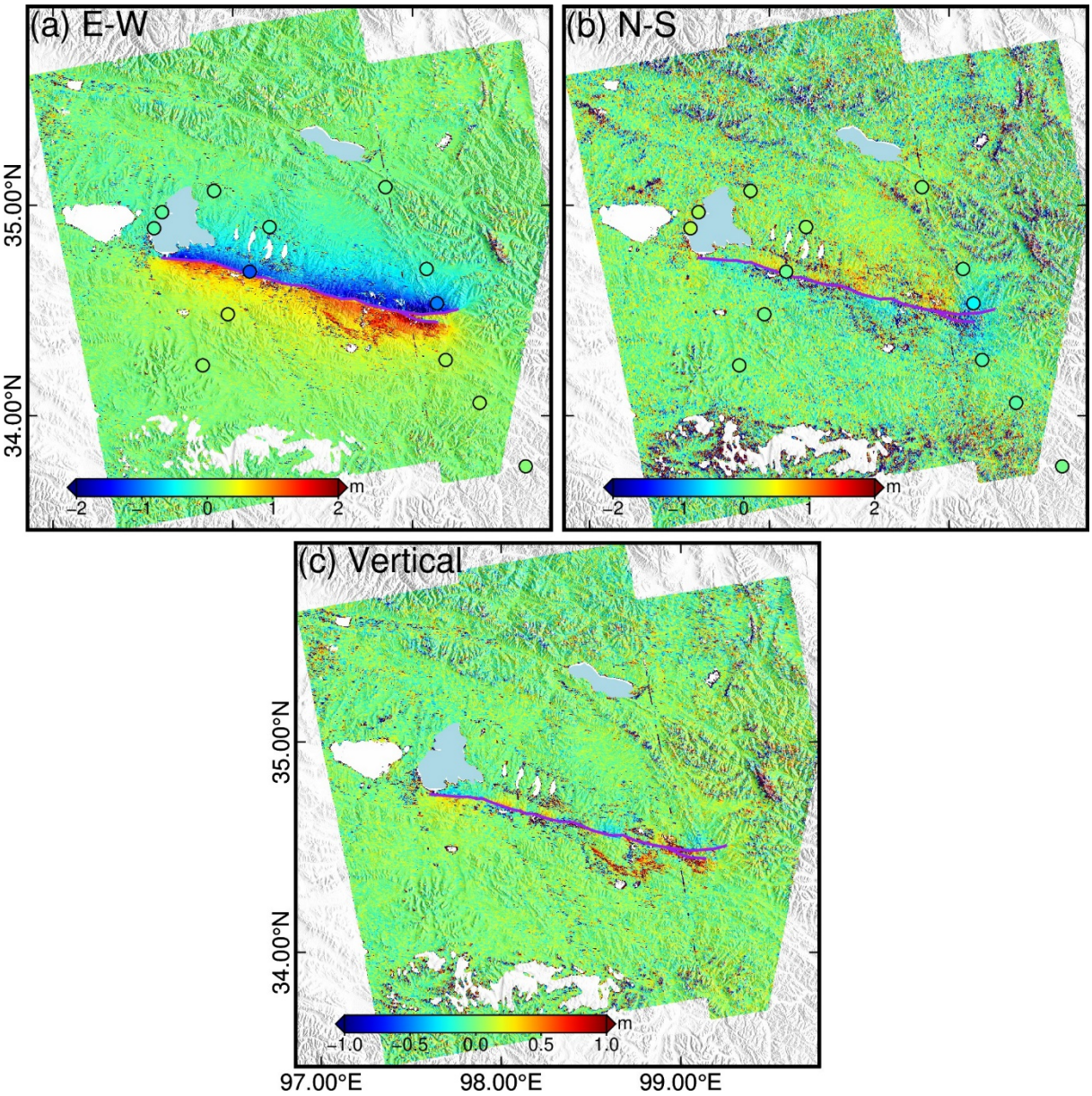

Fig. S3. Three-dimensional displacements of the 2021 Maduo earthquake by the weighted least square (WLS) method. Circles in (a) and (b) show the locations of the GNSS stations, and their color indicates the GNSS-observed displacement. As can be seen, the WLS result is much noisier compared with the SM-VCE result (Fig. S4).

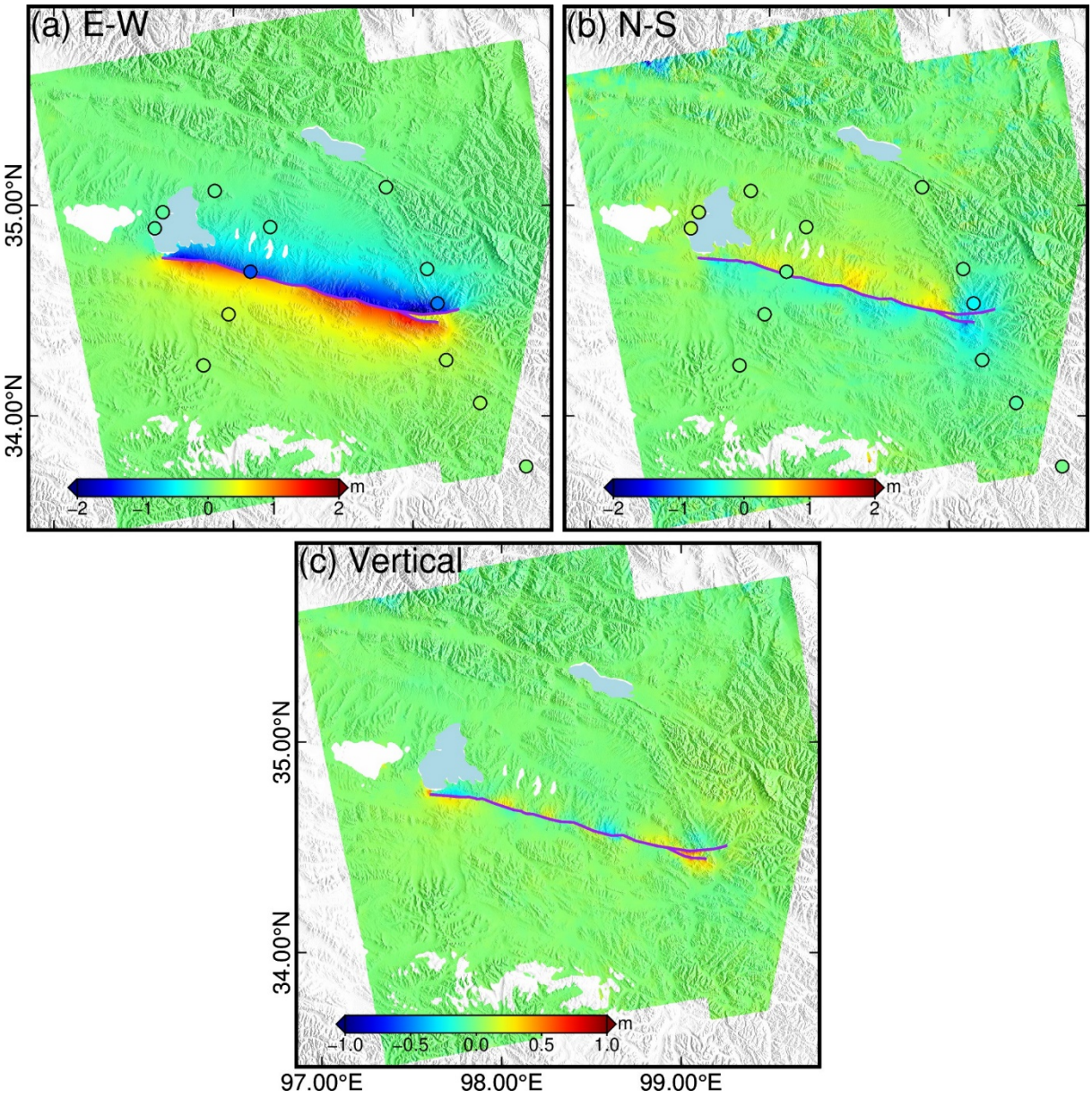

Fig. S4. Three-dimensional displacements of the 2021 Maduo earthquake by SM-VCE method. Circles in (a) and (b) show the locations of the GNSS stations, and their color indicates the GNSS-observed displacement. The enlarged view of the displacements near the fault can be found in the main text.

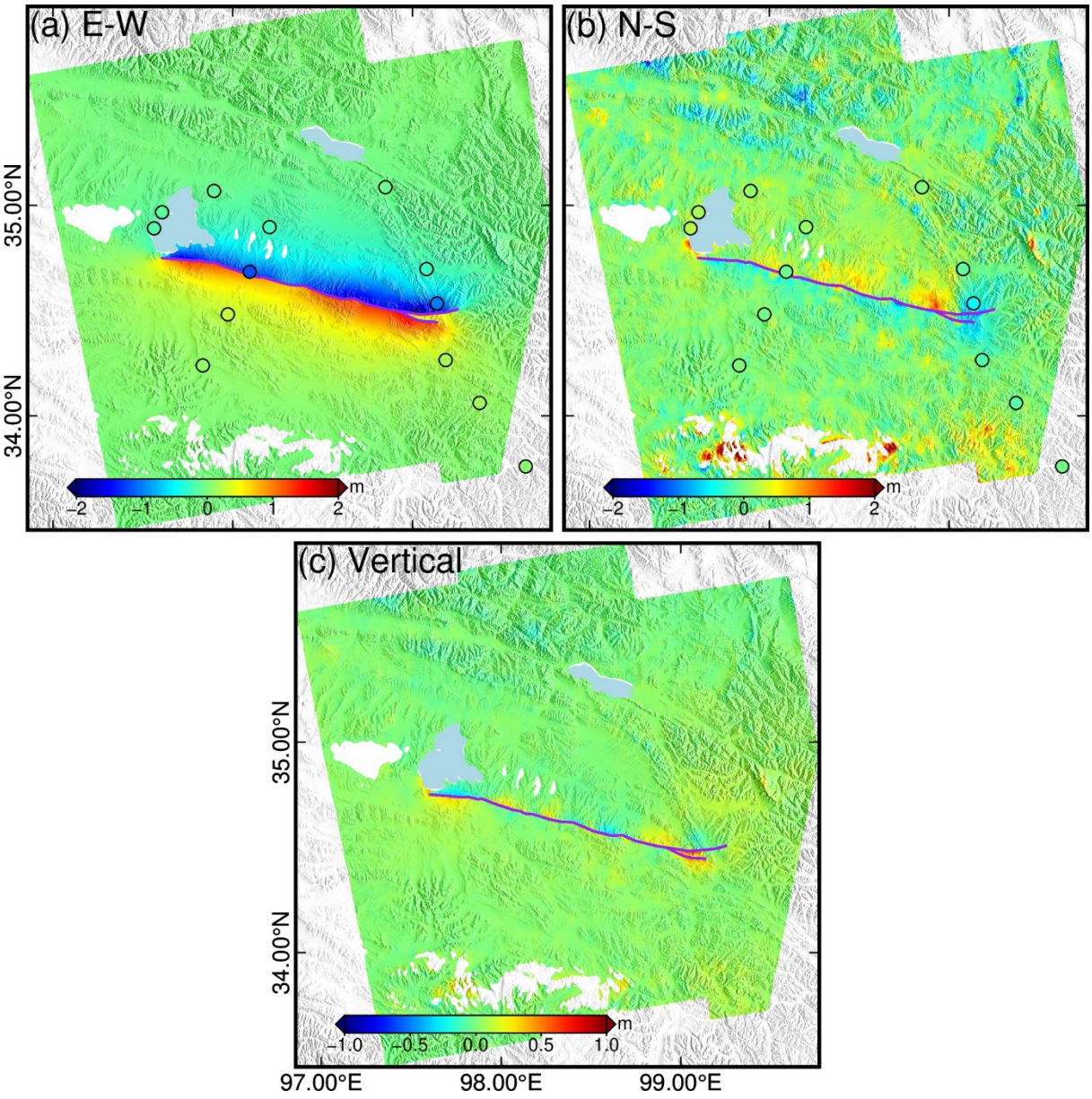

Fig. S5. Similar as Fig. S4 but without using the BOI observations. Compared with Fig. S4, the N-S displacement component without the BOI observations is much noisier. Comparison with the GNSS data demonstrates the significance of the BOI observations for calculating accurate N-S displacement.

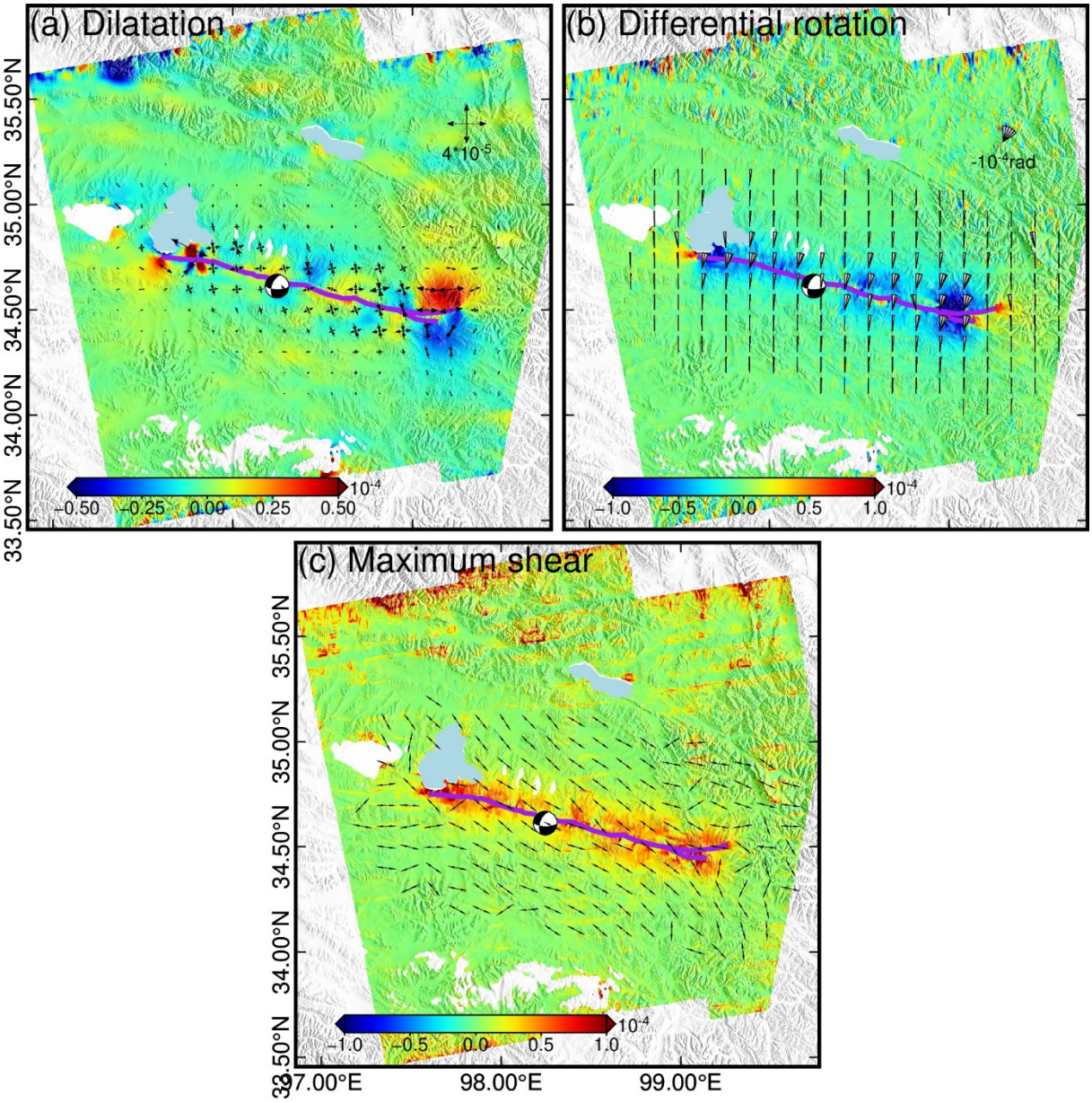

Fig. S6. Three strain invariants for the 2021 Maduo earthquake. In (a), the crosses represent the maximum and minimum normal strains, where the arrow orientation and the arrow length are the direction and magnitude of the strains, respectively. The extensional and compressional strains are shown as the inward and outward arrows, respectively. In (b), the rotational wedges are presented to better illuminate the magnitude and direction of the rotation. In (c), the direction of the double-sided arrow represents the direction of the maximum shear. The enlarged view of the strain fields near the fault can be found in the main text.

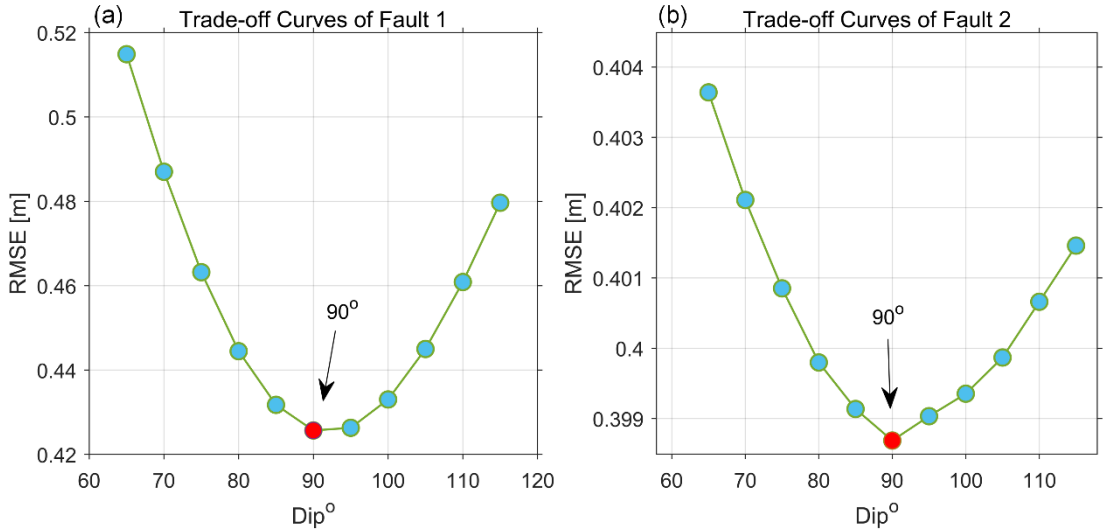

Fig. S7. Dipping angle determination for two deducted faults. (a) fault one. (b) fault two. Both of the searched optimal dipping angles are all 90 degrees.

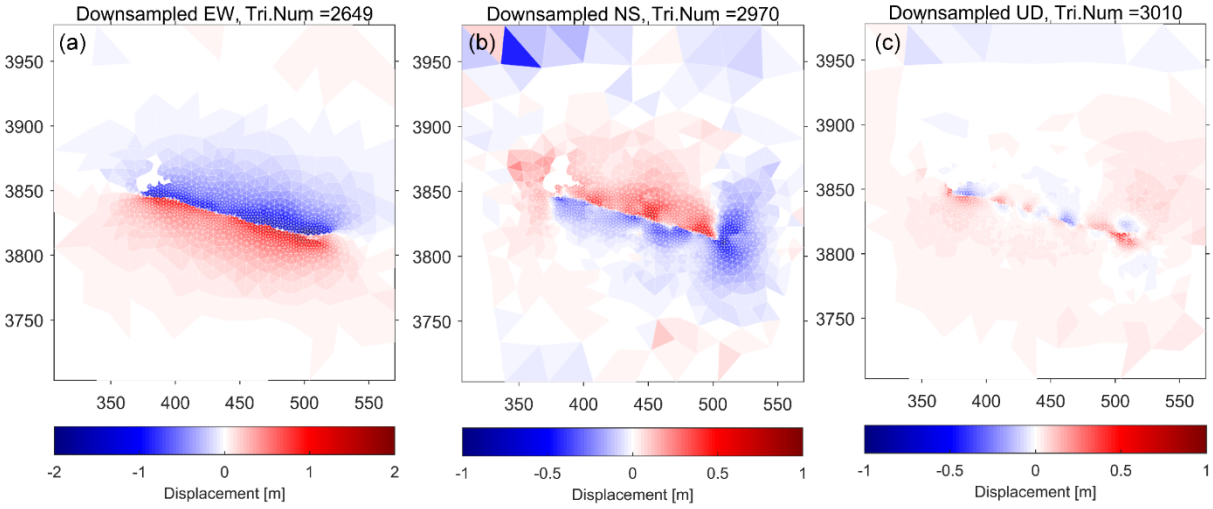

Fig. S8. Downsampled 3-D displacements using fault-geometry as a constraint. (a-c) are the downsampled displacements of east-west (E-W), north-south (N-S) and vertical components, respectively.

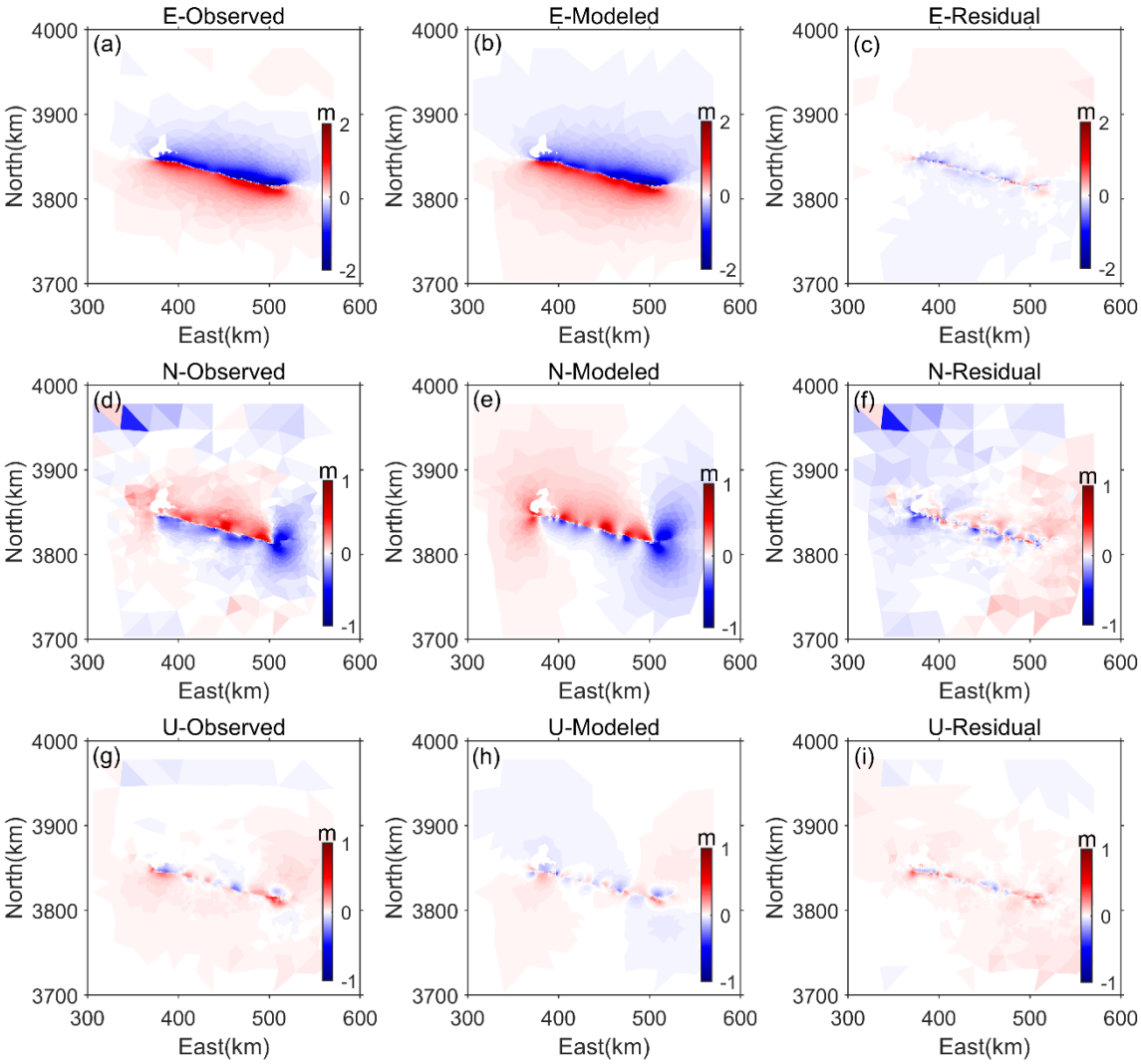

Fig. S9. The derived 3-D displacements, the modeled coseismic displacements and their corresponding residuals. (a-c) are respectively the derived E-W displacement, modeled displacement and model residuals. (d-e) are respectively the derived N-S components and (f-i) are the corresponding components for vertical component.

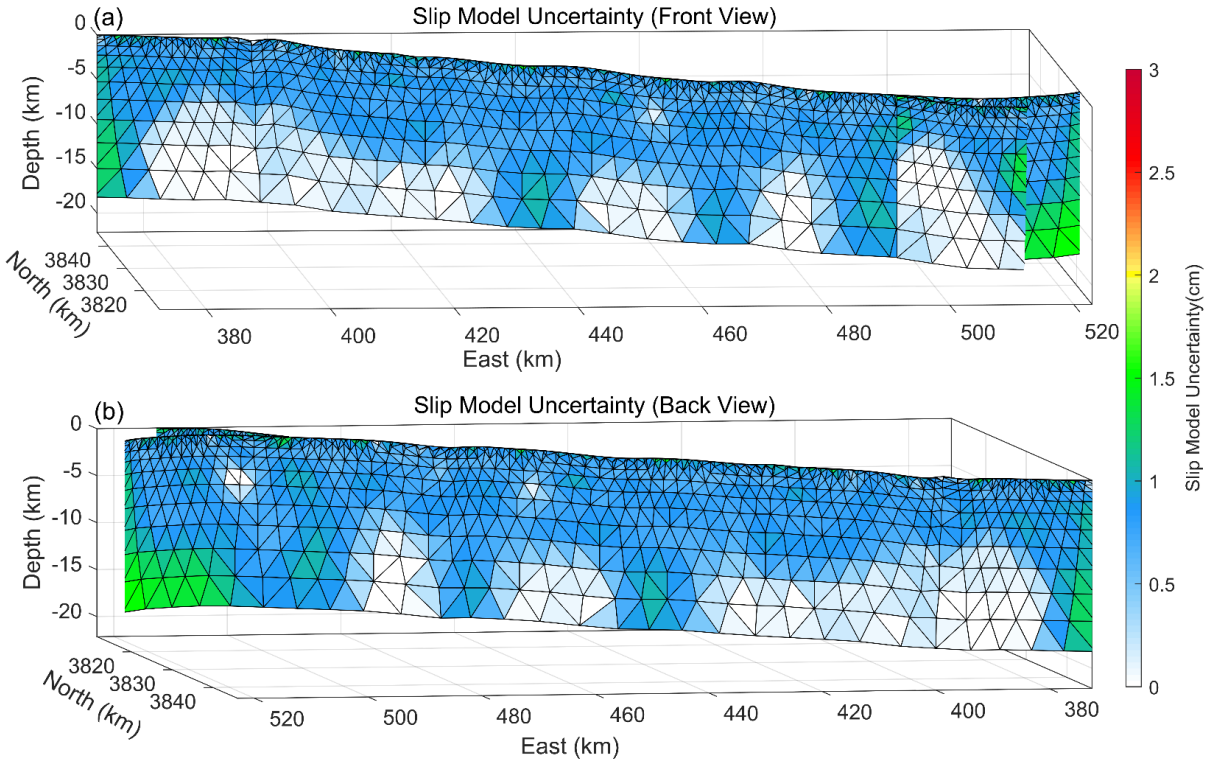

Fig. S10. The model uncertainty of the inverted slip distribution due to possible random noise in our derived 3-D displacements observations. (a) front view (b) back view.

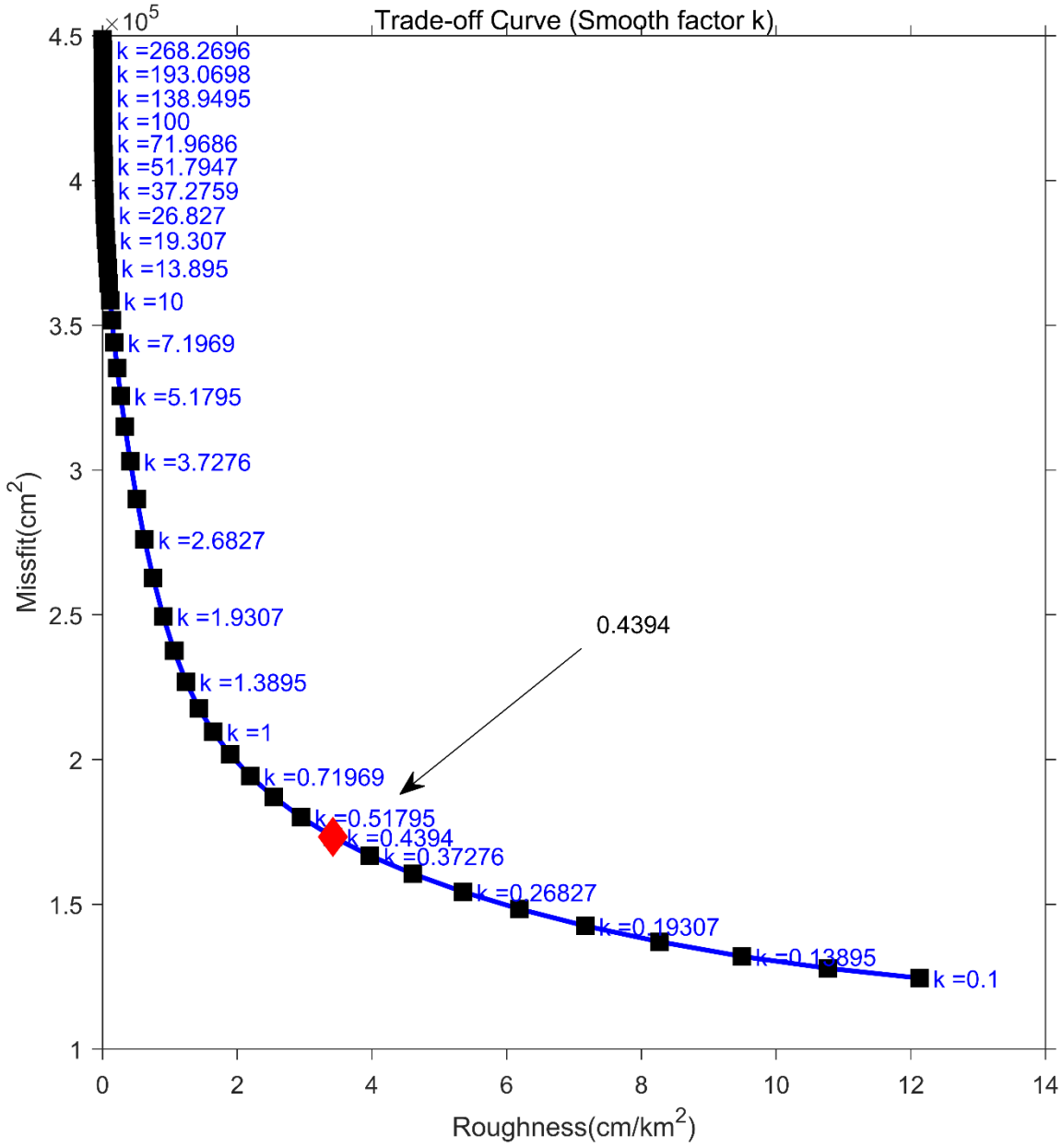

Fig. S11. The trade-off curve used for estimating the optimal smoothing factor. The automatically selected best smooth factor is 0.4394.

References

[1] Grandin R, Klein E, Métois M, et al. 3d displacement field of the 2015 m w 8.3 illapel earthquake (chile) from across- and along-track sentinel-1 tops interferometry. Geophys Res Lett 2016;43:2552-2561.

[2] Gabriel AK, Goldstein RM, Zebker HA. Mapping small elevation changes over large areas: Differential radar interferometry. J Geophys Res Solid Earth 1989;94:9183-9191.

[3] Bechor NBD, Zebker HA. Measuring two-dimensional movements using a single insar pair. Geophys Res Lett 2006;33:275-303.

[4] Michel R, Avouac JP, Taboury J. Measuring ground displacements from sar amplitude images: Application to the landers earthquake. Geophys Res Lett 1999;26:875-878.

[5] Li Z, Ding X, Huang C, et al. Improved filtering parameter determination for the goldstein radar interferogram filter. ISPRS J Photogramm Remote Sens 2008;63:621-634.

[6] Chen CW, Zebker HA. Phase unwrapping for large sar interferograms: Statistical segmentation and generalized network models. IEEE Trans Geosci Remote Sens 2002;40:1709-1719.

[7] Hu J, Yang W, Liu J, et al. Correcting ionospheric error for mai based on along-track gradient and 1-d linear fitting. IEEE Geosci Remote Sens Lett 2021:1-5.

[8] Gomba G, Parizzi A, Zan FD, et al. Toward operational compensation of ionospheric effects in sar interferograms: The split-spectrum method. IEEE Trans Geosci Remote Sens 2016;54:1446-1461.

[9] Gomba G, Gonzalez FR, Zan FD. Ionospheric phase screen compensation for the sentinel-1 tops and alos-2 scansar modes. IEEE Trans Geosci Remote Sens 2016;55:223-235.

[10] Wegmüller U, Werner C, Strozzi T, et al. Sentinel-1 support in the gamma software. Procedia Comput Sci 2016;100:1305-1312.

[11] Guglielmino F, Nunnari G, Puglisi G, et al. Simultaneous and integrated strain tensor estimation from geodetic and satellite deformation measurements to obtain three-dimensional displacement maps. IEEE Trans Geosci Remote Sens 2011;49:1815-1826.

[12] Wang X, Liu G, Yu B, et al. 3d coseismic deformations and source parameters of the 2010 yushu earthquake (china) inferred from dinsar and multiple-aperture insar measurement. Remote Sens Environ 2014;152:174-189.

[13] Wang X, Liu G, Yu B, et al. An integrated method based on dinsar, mai and displacement gradient tensor for mapping the 3d coseismic deformation field related to the 2011 tarlay earthquake (myanmar). Remote Sens Environ 2015;170:388-404.

[14] Hu SW, Xiao BL. Modern theory and application of surveying data processing (in chinese). Beijing, China: Surveying and Mapping Press, 2016

[15] Liu J, Hu J, Xu W, et al. Complete three-dimensional co-seismic deformation fields of the 2016 central tottori earthquake by integrating left- and right-looking insar with the improved sm-vce method. J Geophys Res Solid Earth 2019;124:12099–12115.

[16] Fialko Y, Jin Z. Simple shear origin of the cross-faults ruptured in the 2019 ridgecrest earthquake sequence. Nat Geosci 2021:1-6.

[17] Lohman RB, Barnhart WD. Evaluation of earthquake triggering during the 2005–2008 earthquake sequence on qeshm island, iran. J Geophys Res Solid Earth 2010;115.

[18] Lohman RB, Simons M. Some thoughts on the use of insar data to constrain models of surface deformation: Noise structure and data downsampling. Geochem Geophys Geosyst 2005;6.

[19] Meade BJ. Algorithms for the calculation of exact displacements, strains, and stresses for triangular dislocation elements in a uniform elastic half space. Comput Geosci 2007;33:1064-1075.

[20] Hansen PC. Regularization tools: A matlab package for analysis and solution of discrete ill-posed problems. Numerical algorithms 1994;6:1-35.

[21] Khoshmanesh M, Shirzaei M, Nadeau RM. Time-dependent model of aseismic slip on the central san andreas fault from insar time series and repeating earthquakes. J Geophys Res Solid Earth 2015;120:6658-6679.